High-Resolution Magnetic Resonance Angiography in the Mouse Using a Nanoparticle Blood-Pool Contrast Agent

Gabriel P. Howles, **Ketan B. Ghaghada**, **Yi Qi**, **Srinivasan Mukundan Jr.**, and **G. Allan Johnson**
Center for In Vivo Microscopy, Department of Radiology, Duke University Medical Center, Durham, North Carolina, USA

Abstract

High-resolution magnetic resonance angiography is already a useful tool for studying mouse models of human disease. Magnetic resonance angiography in the mouse is typically performed using time-of-flight) contrast. In this work, a new long-circulating blood-pool contrast agent—a liposomal nanoparticle with surface-conjugated gadolinium (SC-Gd liposomes)—was evaluated for use in mouse neurovascular magnetic resonance angiography. A total of 12 mice were imaged. Scan parameters were optimized for both time-of-flight and SC-Gd contrast. Compared to time-of-flight contrast, SC-Gd liposomes (0.08 mmol/kg) enabled improved small-vessel contrast-to-noise ratio, larger field of view, shorter scan time, and imaging of venous structures. For a limited field of view, time-of-flight and SC-Gd were not significantly different; however, SC-Gd provided better contrast-to-noise ratio when the field of view encompassed the whole brain ($P < 0.001$) or the whole neurovascular axis ($P < 0.001$). SC-Gd allowed acquisition of high-resolution magnetic resonance angiography ($52 \times 52 \times 100$ micrometer^3 or 0.27 nL), with 123% higher ($P < 0.001$) contrast-to-noise ratio in comparable scan time (~45 min). Alternatively, SC-Gd liposomes could be used to acquire high-resolution magnetic resonance angiography (0.27 nL) with 32% higher contrast-to-noise ratio ($P < 0.001$) in 75% shorter scan time (12 min).

Abnormal vascular morphology is associated with numerous cerebral diseases. These diseases span a wide range from vasculopathies such as atherosclerosis to neurodegenerative conditions such as Alzheimer's disease to neoplastic diseases such as glioblastoma multiforme. In the clinical domain, magnetic resonance angiography (MRA) has become one of the most valuable tools for evaluating both normal and pathologic vascular anatomy. MRA is well suited to studying vascular architecture because it provides excellent vessel contrast while being noninvasive and inherently three-dimensional (3D). In the preclinical domain, MRA is also being adopted to study corresponding animal models of human diseases. In mouse models of neurologic and neoplastic diseases, subtle changes in vascular morphology have been found to be relevant to the disease process (1,2). MRA of mouse models has been used in the study of middle cerebral artery occlusion (3), vascular changes associated with Alzheimer's disease (2,4), collateral flow in peripheral vascular occlusion (5), and vascularity in choroid plexus carcinoma (6).

To date, the highest-resolution mouse MRA studies have used 3D time-of-flight (TOF) contrast acquired with 3D gradient echo sequences (3,6). In this approach, the vessel signal comes primarily from unsaturated blood flowing into the field of view (FOV) (inflow enhancement), so it provides superb visualization of the large and proximal arteries in a particular FOV. However, because the inflowing spins are rapidly saturated by the rapid pulse repetition, no

*Correspondence to: G. Allan Johnson, XX, Center for In Vivo Microscopy, Box 3302, Duke University Medical Center, Durham, NC 27710. gjohnson@duke.edu.

signal remains for visualizing the distal arteries and/or venous circulation. This loss of distal vessel signal becomes problematic in regions with turbulent or slow flow or with tortuous vessels, such as in the brain and tumors (4). This problem is exacerbated when the large arteries supplying a region are included in the FOV.

Contrast agents can be used in MRA to increase small-vessel contrast. In contrast-enhanced MRA (CE-MRA), the vessel signal comes not only from the TOF effect but also from magnetization that recovers in the blood due to T_1-shortening by the contrast agent. However, conventional low-molecular-weight contrast agents, such as Gd-DTPA, rapidly extravasate from the vascular space. As a result, the time window for imaging is considerably reduced, thus limiting acquisition of high-resolution images (7–9). Several macromolecular and nanoparticle-based contrast agents have been developed (10) to overcome these limitations with conventional contrast agents. Recently, long-circulating gadolinium contrast agents have been developed using a liposomal platform (8,11). The nanoscale size of the liposomes (50–200 nm) limits their extravasation from the vasculature, making them a "blood-pool" contrast agent. In addition, the liposomes are coated with polyethylene glycol, which slows the clearance rate and gives these agents a long in vivo residence time. These blood-pool and long-circulating features permit an extended time window for imaging, which allows acquisition of high-spatial-resolution images (12–14).

The first generation of these liposomal contrast agents carried gadolinium within the liposomal core. We have now created a second generation of agents, in which the gadolinium is conjugated to the surface of the liposome (*surface-conjugated* or SC-Gd liposomes). Compared to core-encapsulated liposomes, SC-Gd liposomes have approximately twice the T_1 relaxivity (at 7 T), because the lanthanide center is presented on the surface of the liposomes and is thus allowed more interactions with the blood protons.

In this study, the utility of SC-Gd liposomes for CE-MRA was evaluated for neurovascular imaging in the mouse. Because the best mouse MRA results to date have utilized TOF-MRA (3,6), TOF-MRA was used as the reference standard for quantitative assessment. First, a TOF-MRA protocol was optimized to establish benchmarks of spatial resolution, small-vessel contrast, FOV, and scan time. Then, a corresponding CE-MRA protocol using SC-Gd liposomes was developed and compared to determine if the contrast agent could improve neurovascular mouse MRA in terms of small-vessel contrast, FOV, spatial resolution, and scan time.

MATERIALS AND METHODS

Preparation of SC-Gd Liposomes

A lipid mixture consisting of 1,2-dipalmitoyl-*sn*-glycero-3-phosphocholine (Genzyme, MA), Gd-DTPA bis(stearyl-amide) (Gd-DTPA-bovine serum albumin) (IQsynthesis, St. Louis, MO), cholesterol (Sigma-Aldrich, St. Louis, MO) and 1,2-distearoyl-*sn*-glycero-3-phosphoethanolamine-N-[methoxy(poly(ethylene glycol))-2000] (Genzyme) in the ratio 32:25:40:3 was dissolved in a chloroform:methanol mixture. The solvent mixture was evaporated to dryness under vacuum, and the lipid contents were hydrated with a solution of 150-mM saline. The solution was stirred for 2 h at 60°C and then sequentially extruded with three passes through a 400-nm Nuclepore membrane (Waterman, Newton, MA), five passes through a 200-nm Nuclepore membrane, seven passes through a 100-nm Nuclepore membrane, and 10 passes through a 50-nm Nuclepore membrane.

The size distribution of liposomes was determined by dynamic light scattering using a ZetaPlus Analyzer (Brookhaven Instruments, Chapel House, UK). The gadolinium content of SC-Gd liposomes was quantified using inductively coupled plasma optical emission spectroscopy

(Model Optima 4300D; PerkinElmer, Norwalk, CT) operating at a wavelength of 336.223 nm for gadolinium. The T_1 molar relaxivity in bovine plasma was measured at 7 T, as previously described (11). For this work, two different batches of SC-Gd were used.

Animal Handling and MRI

All animal studies were approved by the Duke University Institutional Animal Care and Use Committee. Twelve male C57BL/6 mice (25–28 g) were used for the study; each mouse was sacrificed after a single session of imaging. Free-breathing mice were anesthetized with isoflurane delivered by nose cone. The nose cone was specially designed to fix the head precisely in the "flat skull" position. Throughout the experiments, the animals' respiratory rate and rectal temperature were monitored. The respiratory rate was maintained between 85 and 125 breaths per minute by titrating the isoflurane concentration. Rectal temperature was maintained at $35.9 \pm 0.1°C$ with a blown-air feedback system. For MR imaging, the animals were placed in a 35-mm-diameter quadrature volume coil (m2m Imaging Corp., Cleveland, OH), which was used for both transmit and receive. Imaging studies were performed on a 7-T Magnex magnet interfaced to a Signa EXCITE console (version 12.4; GE Medical Systems, Milwaukee, WI). All CE images were acquired within 6 h of injection of the contrast agent. In preliminary work, contrast enhancement was found to be stable for at least 8 h after injection.

Optimization of TOF-MRA

To find the optimum combination of parameters for TOF-MRA, pulse repetition time (TR) and flip angle (FA) were systematically varied ($n = 3$ mice). The longest TR (80 ms) was chosen, so that the maximum scan time of a high-resolution scan (described later) would be approximately 45 min. For TRs less than 80 ms, the number of excitations (NEX) was adjusted to maintain a constant scan time. Because the TOF contrast depends on inflowing unsaturated spins, a small, axially oriented FOV was selected (FOV 1 in Fig. 1a) to minimize the excitation of the large arteries supplying the brain. A 3D spoiled gradient recalled echo sequence (SPGR) was used with the following parameters: FOV = $20 \times 15 \times 6$ mm; matrix = $256 \times 96 \times 60$; echo time (TE) = 3 ms; TR = 20, 40, or 80 ms; FA = 10, 20, 40, 60, or 80°; NEX = 4, 2, or 1 (to maintain constant scan time); receive bandwidth (BW) = 15.63 kHz. The data were zero-filled and reconstructed at $256 \times 256 \times 60$. Image analysis was performed as described below on the azygous anterior cerebral artery (AzACA).

Optimization of CE-MRA

To find the optimum combination of parameters for CE-MRA, TR and FA were systematically varied. Prior to imaging, SC-Gd liposomes were administered by tail vein at a dose of 0.04 ($n = 2$) or 0.08 ($n = 2$) mmol Gd per kg bodyweight. Because the goal was to optimize the parameters for CE-MRA, we sought to minimize the contribution of TOF effects to the vessel signal. Therefore, a large and longitudinally oriented FOV (similar to FOV 3 in Fig. 1a) was selected to excite the blood in the large arteries of the neck and thorax. The parameters for the 3D SPGR sequence were FOV = $26 \times 26 \times 11.2$ mm; matrix = $128 \times 128 \times 56$; TE = 3 ms (minimum possible); FA = 10, 20, 30, 40, or 60; TR = 20, 40, or 80 ms; NEX = 4, 2, or 1; BW = 15.63 kHz. The data were zero-filled and reconstructed at $256 \times 256 \times 56$. Image analysis was performed as described below on the AzACA and also on the straight sinus (a vein).

Effect of SC-Gd Liposome Dose on Contrast-to-Noise Ratio

To evaluate the dose-effect of SC-Gd, CE-MRA were acquired with four different doses of SC-Gd liposomes: 0, 0.02, 0.04, and 0.08 mmol Gd per kg bodyweight ($n = 1$). A fixed TR was used with three different FAs. The parameters for the 3D SPGR sequence were FOV = 20 $\times 15 \times 6$ mm; matrix = $256 \times 96 \times 60$; TE = 3 ms (minimum possible); FA = 20, 40, or 60°; TR = 20 ms; NEX = 4; BW = 15.63 kHz. The data were zero-filled and reconstructed at 256

$\times 256 \times 60$. To completely isolate the SC-Gd liposome dose effect from any TOF effects, image analysis was performed (as described later) on a 0.5-mm segment of a large vein—the superior sagittal sinus.

Effect of FOV

To examine the effect of FOV on CE-MRA, images were acquired using both optimized TOF-MRA ($n = 1$) and optimized CE-MRA ($n = 1$) parameters at three different FOV (Fig. 1). FOV 1 covered only a narrow axial slab of the brain. FOV 2 encompassed the whole brain. FOV 3 covered the entire neurovascular axis, including the large vessels of the neck and the arch of the aorta. For CE-MRA, SC-Gd liposomes were administered by tail vein at 0.08 mmol Gd per kg bodyweight. All MRA were acquired at approximately 100–μm isotropic spatial resolution. Because the optimum TR was different for each contrast mechanism, NEX were adjusted to keep the total scan time constant for a given FOV. BW = 15.63 kHz. The remaining SPGR imaging parameters are provided in Table 1.

High-Resolution MRA

Using the optimized scan parameters, high-resolution MRA of the whole brain (FOV 2 in Fig. 1a) was acquired with both TOF-MRA and CE-MRA. For CE-MRA, SC-Gd liposomes were administered at a dose of 0.08 mmol Gd per kg. Data were acquired at a Nyquist resolution of $52 \times 52 \times 100 \ \mu m^3$ and zero-filled and reconstructed with a voxel size of $39 \times 39 \times 100 \ \mu m^3$. For TOF-MRA the parameters were TR = 80 ms; FA = 60°; NEX = 1 ($n = 9$). For CE-MRA the parameters were TR = 22 ms; FA = 20°; NEX = 4 ($n = 5$), 2 ($n = 1$), or 1 ($n = 1$). For all scans, matrix = $384 \times 384 \times 80$; FOV = $20 \times 20 \times 8 \ mm^3$. For almost all scans, TE = 3 ms and BW = 31.25; however, for the final set TOF and CE-MRA, TE = 4 ms, and BW = 17.66 kHz. (This latter combination was found to provide marginally higher signal-to-noise ratio [SNR] and contrast-to-noise ratio [CNR].)

Image Analysis

Image analysis was performed using ImageJ (v.1.40, National Institutes of Health, http:/rsb.info.nih.gov/ij/) and MATLAB (The MathWorks, Natick, MA). For the analysis, a distal segment of the AzACA was selected. This segment was 0.5 mm long and was oriented parallel with the rostral-caudal axis of the brain. Axial images were selected that were perpendicular to the vessel segment. In each of the image slices intersecting this vessel segment, three regions of interest (ROIs) were selected: (1) an ROI surrounding vessel; (2) an ROI encompassing background brain tissue without discernable vessels or cerebral ventricles; and (3) a large ROI of background noise away from the specimen. The vessel signal was measured as the maximum image intensity in the vessel ROI because the vessels analyzed were so small (often only single voxel in a slice). The tissue signal was the measured as the mean image intensity in the tissue ROI. The noise was measured as the standard deviation of the image intensity in the noise ROI. SNR and CNR measurements were made for the vessel and tissue in each slice passing through the 0.5-mm segment of the AzACA. (Note that because the resolution of the scans varied, the number of slices through this 0.5-mm segment varied accordingly.) The mean and SE of these measurements are reported on all figures. Statistical comparisons were made by pooling all slice measurements from all the datasets in a given sample group and performing independent two-tailed *t* tests (variance was not assumed to be equal).

RESULTS

SC-Gd Characterization

The mean size of the SC-Gd liposomes was 75.9 nm (standard deviation 10.0 nm). The mean gadolinium content was 14.57 mM. The molar relaxivity in bovine plasma at 7 T was 3.3 $mM^{-1}s^{-1}$ (standard deviation 0.17 $mM^{-1}s^{-1}$).

Optimization of TOF-MRA

To optimize TOF-MRA, vessel measurements were made at several combinations of TR (20–80 ms) and FA (10–80°), with NEX adjusted to maintain a constant scan time ($n = 3$). The minimum TE was chosen to maximize the SPGR signal. Because the TOF contrast depends on inflowing unsaturated spins, a small axial FOV was selected (FOV 1 in Fig. 1a) to minimize the excitation of the large arteries (e.g., the internal carotid artery) supplying the brain.

The proximal arteries of the brain (e.g., proximal segments of the middle cerebral and anterior cerebral arteries) have relatively high flow and are very close to the large supplying arteries. As a result, these vessels have excellent conspicuity at any combination of FA and TR (data not shown). However, optimization of parameters is important for visualizing the small, distal arteries. Therefore, a small distal segment of the AzACA was chosen for SNR/CNR measurements.

For each TR value, an optimum FA was obtained that resulted in maximum SNR for the blood vessel (Fig. 2a). The optimum FA was higher for longer TRs. For background tissue signal, typical SPGR relationships between SNR and FA or TR were observed (Fig. 2b). SNR decreased with shorter TR and higher FA (beyond the Ernst angle). CNR plots demonstrated that the optimum vessel conspicuity was obtained with a TR of 80 ms and an FA of 60° (Fig. 2c). While a longer TR might have offered still greater CNR, the maximum TR of 80 ms had been chosen a priori, so that the high-resolution acquisition (described previously) would not exceed 45 min.

Optimization of CE-MRA

To optimize CE-MRA, a minimum TE was chosen and TR and FA were systematically varied. NEX were adjusted to keep the total scan time constant ($n = 4$). To minimize the contribution of unsaturated spins (TOF contrast) to the MRA, the FOV was chosen to be large and longitudinally oriented so as to encompass the large vessels of the neck. Using this large FOV, the blood was expected to be at least partially saturated by the time it reached the AzACA. A small distal segment of the AzACA was again analyzed.

For each TR, there was an optimum FA that maximized the vessel SNR (Fig. 3a). The peak vessel SNR was obtained with a TR of 20 ms and an FA of 20°. As seen in the TOF optimization discussed above, background tissue SNR decreased with shorter TR and higher FA (beyond the Ernst angle) (Fig. 3b). Combining the vessel and brain measurements in the CNR calculation indicated that the SC-Gd contrast was optimum at a TR of 20 ms and an FA of 20–30° (Fig. 3c).

To confirm that there was minimal contribution of TOF contrast to these MRA, the analysis was repeated on a vein. Because venous blood passes slowly through the capillary beds, the magnetization of the venous blood can be expected to be at steady state. Thus, venous vascular contrast should reflect the effects of contrast agent without any TOF contrast. The results (not shown) from the straight sinus (a medium-sized cranial vein) were very similar to those from the AzACA: CE-MRA was optimum at a TR of 20 ms and an FA of 20–30°.

For comparison, the Ernst angles to optimize the SPGR signal from nonflowing plasma were calculated for TRs of 20, 40, and 80 ms and found to be 25.9°, 35.9°, and 49.0°, respectively. These calculations were based on a plasma volume of 0.05 L/kg (15), an SC-Gd dose of 0.08 mmol/kg, and an SC-Gd molar relaxivity in plasma of 3.3 $mM^{-1}s^{-1}$.

Effect of SC-Gd Liposome Dose on Vessel CNR

To assess the effect of SC-Gd liposome dose on the vessel contrast, four different doses were evaluated: 0, 0.02, 0.04, and 0.08 mmol/kg. The optimum TR found in the previous experiment (20 ms) was used with four different FA. To isolate the effect of contrast agent from TOF effects, the CNR analysis was performed on a vein: the superior sagittal sinus (Fig. 4). Over the range of doses tested, the CNR improved with increasing dose. However, the relative benefit of increasing dose was greater between 0 and 0.04 mmol/kg than between 0.04 and 0.08 mmol/ kg.

For reference, the Ernst angles to optimize the SPGR signal (TR = 20 ms) from nonflowing plasma were calculated for the doses 0.02, 0.04, and 0.08 mmol/kg and found to be 13.1°, 18.5°, and 25.9°, respectively. These calculations were based on a plasma volume of 0.05 L/ kg (15) and an SC-Gd molar relaxivity in plasma of 3.3 $mM^{-1}s^{-1}$.

Effect of FOV

To examine the effects of FOV on TOF-MRA and CE-MRA, scans were acquired using optimized parameters at three different FOVs (Fig. 1a). Maximum intensity projections (MIPs) were generated to demonstrate the effect of FOV on each contrast mechanism (Fig. 5). Corresponding CNR measurements of the AzACA were also performed (Fig. 6a).

The TOF-MRA at FOV 1 showed excellent arterial contrast, which exceeded that of the CE-MRA. However, as the FOV increased, the image quality of TOF-MRA degraded, even though these larger FOVs had longer total scan times. Despite this degradation, the whole brain TOF-MRA at FOV 2 still demonstrated the small vessels with high conspicuity. However, in the TOF-MRA at FOV 3, contrast was lost in most small vessels. On the other hand, CE-MRA appeared to be insensitive to FOV, permitting visualization of both large and small vessels simultaneously. In fact, the vessel CNR improved (as expected, $P < 0.001$) as the volume of excitation and total scan time increased (Fig. 6a).

In TOF-MRA, it may be possible to improve vessel contrast by lengthening TR and thus give more time for vessel refilling. We attempted to recover small-vessel contrast in TOF-MRA at FOV 3 by using longer TRs (160 and 320 ms). However, with these longer TRs and an FA of 90°, the increase in background tissue signal overwhelmed any improvements in vessel signal (data not shown).

High-Resolution MRA

TOF-MRA and CE-MRA of the whole brain (FOV 2 in Fig. 1a) were acquired with optimized parameters at a spatial resolution of $52 \times 52 \times 100$ μm^3 (0.27 nL) (Fig. 7a,b). The CE-MRA was acquired with 4 NEX to match the scan time of the TOF-MRA. CNR measurements of the AzACA in these high-resolution scans were compared (Fig. 6b) to corresponding measurements from the $104 \times 104 \times 100$ μm^3 images (1 nL) (Fig. 5c,d). At 1-nL resolution, CE-MRA ($n = 1$) had 36% better ($P < 0.001$) CNR than TOF-MRA ($n = 1$). When the resolution was increased 4-fold (to 0.27 nL), the CNR decreased for both contrast mechanisms. However, the CNR degraded more for the TOF-MRA than the CE-MRA (compare Fig. 5c,d and Fig. 7a,b). At the higher resolution, SC-Gd ($n = 5$) provided a 123% improvement ($P < 0.001$) in CNR compared to TOF ($n = 9$).

To determine if the benefits of CE-MRA could be used to reduce scan time, high-resolution CE-MRA were also acquired with fewer NEX—1 or 2 NEX instead of 4 NEX. CNR measurements from the AzACA from all the high-resolution scans were compared (Fig. 6c). Compared to the standard TOF-MRA (43 min, $n = 9$), the CE-MRA acquired with 1 NEX (12 min, $n = 1$) had 32% higher CNR ($P < 0.001$); and the CE-MRA with 2 NEX (24 min, $n = 1$) had 90% higher CNR ($P < 0.001$).

Using the optimized MRA techniques allowed visualization of extraordinary anatomic detail. Thin slabs of MIP images of the high-resolution brain datasets were generated to demonstrate some of the fine details of vascular structures (Fig. 7). MIP images of the 1-mm dorsalmost slab of the brain (Fig. 7c,e) demonstrated the most distal branches of the middle cerebral artery. Similarly, MIP images of the 0.3-mm midsagittal slab of brain (Fig. 7d,f) demonstrated the microscopic branches of the anterior spinal artery and basilar artery, which supply the spinal cord and pons. The number and extent of these smallest vessels were greater in the CE-MRA images.

DISCUSSION

We have optimized neurovascular MRA protocols for two different contrast mechanisms: TOF and SC-Gd liposomes. Using the optimized TOF protocol, mouse brain MRA were acquired with excellent contrast at a spatial resolution of $52 \times 52 \times 100$ μm^3 (0.27 nL). To the best of our knowledge, these are the highest resolution TOF-MRA yet acquired. The image quality of MRA was further improved by using the novel intravascular contrast agent, SC-Gd liposomes. Using the optimized CE-MRA protocol, MRA could be acquired with larger FOVs; shorter scan times; and higher small-vessel conspicuity. The relative CNR benefit from the SC-Gd liposomes was greater at higher resolution. In addition, the CE-MRA demonstrated venous anatomy.

Taken alone, the TOF results reported here represent a significant improvement over previous work. The standard for in vivo mouse MRA was set using TOF contrast by Beckman et al. (3) ($100 \times 100 \times 150$ μm^3, or 1.5 nL) and Brubaker et al. (6) ($117 \times 117 \times 117$ μm^3, or 1.6 nL). Though it is difficult to compare image quality between publications, the TOF-MRA reported here have 6-fold higher spatial resolution (0.27 nL). The superior resolution of our TOF-MRA may be attributed to longer scan times (43 min vs 16 min and 23 min) and higher magnet field strength (7 T vs 4.7 T and 3 T). Higher field strength should provide a double benefit for TOF contrast: first, the background tissue has a longer T_1; and second, the inflowing blood has greater magnetization.

Compared to TOF contrast, the potential benefits of long-circulating and/or blood-pool agents have been appreciated for many years. Gd-DTPA-albumin was used for acquisition of rat brain MRA (scan time: 7.27 h) at a spatial resolution $60 \times 60 \times 60$ μm^3 (0.2 nL) (16). However, this protocol is not practical for routine research. Superparamagnetic iron oxide nanoparticles have been used successfully in human MRA (17); however, a study in mice showed only modest benefit for small animal MRA (3). A variety of Gd-labeled dendrimer agents have been developed (7,18,19), which have permitted rapid acquisition of small animal MRA over large FOVs; however, even the highest resolution was only $166 \times 206 \times 320$ μm^3 (11.25 nL) (19). Thus, while there has been interest in long-circulating blood-pool contrast agents, this class of agents has not yet been fully exploited in small-animal MRA.

Our results using SC-Gd liposomes represent a significant improvement over previous small-animal MRA—both TOF and CE. High-resolution CE-MRA (0.27 nL) was acquired with 32% better CNR than the TOF-MRA, but in only 12 min. Though the 12-min CE-MRA scan was superior to the 43-min TOF-MRA, longer CE-MRA acquisitions were possible because SC-

Gd liposomes are a long-circulating blood-pool agent. In comparable scan time, the CE-MRA had 123% CNR advantage. Importantly, the CNR improvement from SC-Gd liposomes was greater at higher resolution and larger FOV.

The images presented here could be further improved by several technical improvements. The RF coil could be improved by using a smaller volume coil, a surface receive coil, or a cryocooled coil. A higher field magnet could have not only increased vessel signal but also suppressed the brain tissue signal by prolonging T_1. Finally, a more sophisticated TOF pulse sequence such as the sliding interleaved KY acquisition could have been used; however, such techniques are not commonly available for small-animal imaging (20).

Recently, Dorr et al. (21) published an exquisite atlas of the mouse brain vasculature, using a 2-h X-ray computed tomography scan of an ex vivo specimen. This atlas, acquired with a resolution of $20 \times 20 \times 20 \ \mu m^3$ (0.008 nL), identifies nearly 70 vessels by name and demonstrates countless unnamed fine branches. While this atlas serves as an unprecedented anatomic reference, the acquisition technique is not feasible for routine in vivo use. The CE-MRA images presented here are 34-fold lower resolution; however, they still are able to demonstrate nearly every named vessel in the Dorr atlas, as well as numerous unnamed branches. Importantly, the CE-MRA protocol can be executed in vivo in less than an hour and is suitable for longitudinal studies.

Compared to CE-MRA, TOF-MRA has the obvious advantage in that it does not require any exogenous agents. Furthermore, TOF-MRA is entirely sufficient when the experiment requires only a limited FOV, relatively low resolution (> 1.5 nL), and relatively large (e.g., carotid arteries) or proximal arteries (e.g., proximal segments of the cerebral arteries). However, the results presented here indicate that long-circulating blood-pool contrast agents may offer significant benefits in certain situations: (a) limited scan time; (b) large FOV; (c) simultaneous imaging of large and small arteries; (d) imaging veins; (e) imaging very small distal arteries; or (f) imaging with high resolution (< 1.5 nL).

Given these strengths of CE-MRA, there are several potential small-animal MRA applications where SC-Gd liposomes may be particularly useful, including models of tumor vasculature, stroke, arteriovenous malformations, and venous thrombosis. Angiogenesis is critical to the cancerous progression of tumors. Consequently, vascular imaging is a valuable tool for studying pathogenesis and treatment of cancer. Because tumors typically hijack small peripheral arteries, the tumor vasculature consists of small distal vessels, for which SC-Gd liposomes offer particular benefit (22).

SC-Gd liposomes may also have a role in stroke research. The most common cause of non-traumatic subarachnoid hemorrhages is rupture of small saccular aneurysms. While mouse models of these cerebral aneurysms exist, the small size of these lesions has limited studies to date to postmortem light microscopy (23). Because agents such as SC-Gd liposomes are able to reliably visualize very small vascular structures, they may allow researchers to study the development of these aneurysms in vivo. Similarly, intraparenchymal hemorrhages most commonly involve deep perforating cerebral vessels (24), which historically have been too small to image in mice. However, using SC-Gd liposomes these perforating cerebral vessels can now be visualized in vivo (Fig. 7), presenting a new opportunity to study this class of hemorrhagic strokes.

Finally, venous thrombosis is a major cause of morbidity and mortality, including pulmonary embolism and cerebral ischemia (25). To study the pathogenesis and treatment, numerous mouse models of hypercoagulability and venous thrombosis have been created (26,27). Because long-circulating agents such as SC-Gd liposomes permit visualization of the venous

structures, they present an opportunity for longitudinal studies of the development, treatment, and sequelae of venous thrombosis.

CONCLUSIONS

MRA of the mouse brain were acquired using either TOF contrast or SC-Gd liposomes, a novel long-circulating blood-pool contrast agent. Using TOF contrast, optimum small-vessel conspicuity was achieved with a TR of 80 ms and an FA of 60°. Using the optimized parameters, high-resolution TOF-MRA ($52 \times 52 \times 100$ μm^3, or 0.27 nL) of the whole brain was acquired in 43 min. Using SC-Gd liposomes, optimum small-vessel conspicuity was achieved with a TR of 20 ms and FA of 20–30°. Using the optimized parameters, high-resolution CE-MRA (0.27 nL) were acquired with superior small-vessel CNR in only 12 min. Alternatively, with comparable scan times, CE-MRA had 123% higher CNR. Compared to TOF contrast, SC-Gd liposomes enabled (a) larger FOVs; (b) shorter scan times; and (c) higher small-vessel conspicuity. In addition, the CE-MRA demonstrated venous anatomy.

Acknowledgments

References

1. Grammas P. A damaged microcirculation contributes to neuronal cell death in Alzheimer's disease. Neurobiol Aging 2000;21:199–205. [PubMed: 10867204]

2. Beckmann N, Schuler A, Mueggler T, Meyer EP, Wiederhold KH, Staufenbiel M, Krucker T. Age-dependent cerebrovascular abnormalities and blood flow disturbances in APP23 mice modeling Alzheimer's disease. J Neurosci 2003;23:8453–8459. [PubMed: 13679413]

3. Beckmann N, Stirnimann R, Bochelen D. High-resolution magnetic resonance angiography of the mouse brain: application to murine focal cerebral ischemia models. J Magn Reson 1999;140:442–450. [PubMed: 10497049]

4. Krucker T, Schuler A, Meyer EP, Staufenbiel M, Beckmann N. Magnetic resonance angiography and vascular corrosion casting as tools in biomedical research: application to transgenic mice modeling Alzheimer's disease. Neurol Res 2004;26:507–516. [PubMed: 15265268]

5. Wagner S, Helisch A, Ziegelhoeffer T, Bachmann G, Schaper W. Magnetic resonance angiography of collateral vessels in a murine femoral artery ligation model. NMR Biomed 2004;17:21–27. [PubMed: 15011247]

6. Brubaker LM, Bullitt E, Yin CY, Van Dyke T, Lin WL. Magnetic resonance angiography visualization of abnormal tumor vasculature in genetically engineered mice. Cancer Res 2005;65:8218–8223. [PubMed: 16166297]

7. Kobayashi H, Sato N, Hiraga A, Saga T, Nakamoto Y, Ueda H, Konishi J, Togashi K, Brechbiel MW. 3D-micro-MR angiography of mice using macromolecular MR contrast agents with polyamidoamine dendrimer core with reference to their pharmacokinetic properties. Magn Reson Med 2001;45:454–460. [PubMed: 11241704]

8. Ayyagari AL, Zhang XD, Ghaghada KB, Annapragada A, Hu XP, Bel-lamkonda RV. Long-circulating liposomal contrast agents for magnetic resonance imaging. Magn Reson Med 2006;55:1023–1029. [PubMed: 16586449]

9. Schwickert HC, Stiskal M, Vandijke CF, Roberts TPL, Mann JS, Demsar F, Brasch RC. Tumor-angiography using high-resolution, 3-dimensional magnetic-resonance-imaging: comparison of gadopentetate dimeglumine and a macromolecular blood-pool contrast agent. Acad Radiol 1995;2:851–858. [PubMed: 9419650]

10. Barrett T, Kobayashi H, Brechbiel M, Choyke PL. Macromolecular MRI contrast agents for imaging tumor angiogenesis. Eur J Radiol 2006;60:353–366. [PubMed: 16930905]

11. Ghaghada K, Hawley C, Kawaji K, Annapragada A, Mukundan S. T1 relaxivity of core-encapsulated gadolinium liposomal contrast agents: effect of liposome size and internal gadolinium concentration. Acad Radiol 2008;15:1259–1263. [PubMed: 18790397]

12. Bucholz E, Ghaghada K, Qi Y, Mukundan S, Johnson GA. Four-dimensional MR microscopy of the mouse heart using radial acquisition and liposomal gadolinium contrast agent. Magn Reson Med 2008;60:111–118. [PubMed: 18581419]

13. Ghaghada, K.; Howles, G.; Qi, Y.; Johnson, G.; Mukundan, S. High-resolution contrast-enhanced magnetic resonance angiography of the mouse circle-of-Willis. Proceedings of the 16th Scientific Meeting, International Society for Magnetic Resonance in Medicine; Toronto. 2008. p. 2234

14. Ghaghada KB, Bockhorst KHJ, Mukundan S, Annapragada AV, Narayana PA. High-resolution vascular imaging of the rat spine using liposomal blood pool MR agent. Am J Neuroradiol 2007;28:48–53. [PubMed: 17213423]

15. Davies B, Morris T. Physiological-parameters in laboratory-animals and humans. Pharm Res 1993;10:1093–1095. [PubMed: 8378254]

16. Mellin AF, Cofer GP, Smith BR, Suddarth SA, Hedlund LW, Johnson GA. 3-Dimensional magnetic-resonance microangiography of rat neurovasculature. Magn Reson Med 1994;32:199–205. [PubMed: 7968442]

17. Anzai Y, Prince MR, Chenevert TL, Maki JH, Londy F, London M, McLachlan SJ. MR angiography with an ultrasmall superparamagnetic iron oxide blood pool agent. J Magn Reson Imaging 1997;7:209–214. [PubMed: 9039617]

18. Kobayashi H, Sato N, Kawamoto S, Saga T, Hiraga A, Ishimori T, Konishi J, Togashi K, Brechbiel MW. 3D MR angiography of intratumoral vasculature using a novel macromolecular MR contrast agent. Magn Reson Med 2001;46:579–585. [PubMed: 11550252]

19. Fink C, Kiessling F, Bock M, Lichy MP, Misselwitz B, Peschke P, Fusenig NE, Grobholz R, Delorme S. High-resolution three-dimensional MR angiography of rodent tumors: morphologic characterization of intratumoral vasculature. J Magn Reson Imaging 2003;18:59–65. [PubMed: 12815640]

20. Liu KC, Rutt BK. Sliding interleaved k(Y) (SLINKY) acquisition: a novel 3D MRA technique with suppressed slab boundary artifact. J Magn Reson Imaging 1998;8:903–911. [PubMed: 9702893]

21. Dorr A, Sled JG, Kabani N. Three-dimensional cerebral vasculature of the CBA mouse brain: a magnetic resonance imaging and micro computed tomography study. Neuroimage 2007;35:1409–1423. [PubMed: 17369055]

22. Taylor JS, Tofts PS, Port R, Evelhoch JL, Knopp M, Reddick WE, Runge VM, Mayr N. MR imaging of tumor microcirculation: promise for the new millennium. J Magn Reson Imaging 1999;10:903–907. [PubMed: 10581502]

23. Morimoto M, Miyamoto S, Mizoguchi A, Kume N, Kita T, Hashimoto N. Mouse model of cerebral aneurysm: experimental induction by renal hypertension and local hemodynamic changes. Stroke 2002;33:1911–1915. [PubMed: 12105374]

24. Schwartz, DT.; Reisdorff, EJ. Emergency radiology. New York: McGraw-Hill, Health Professions Division; 2000. p. xv-672.

25. Stam J. Current concepts: thrombosis of the cerebral veins and sinuses. N Engl J Med 2005;352:1791–1798. [PubMed: 15858188]

26. Dorffler-Melly J, Schwarte LA, Ince C, Levi M. Mouse models of focal arterial and venous thrombosis. Basic Res Cardiol 2000;95:503–509. [PubMed: 11192373]

27. Rottger C, Bachmann G, Gerriets T, Kaps M, Kuchelmeister K, Schachenmayr W, Walberer M, Wessels T, Stolz E. A new model of reversible sinus sagittalis superior thrombosis in the rat: magnetic resonance imaging changes. Neurosurgery 2005;57:573–579. [PubMed: 16145538]
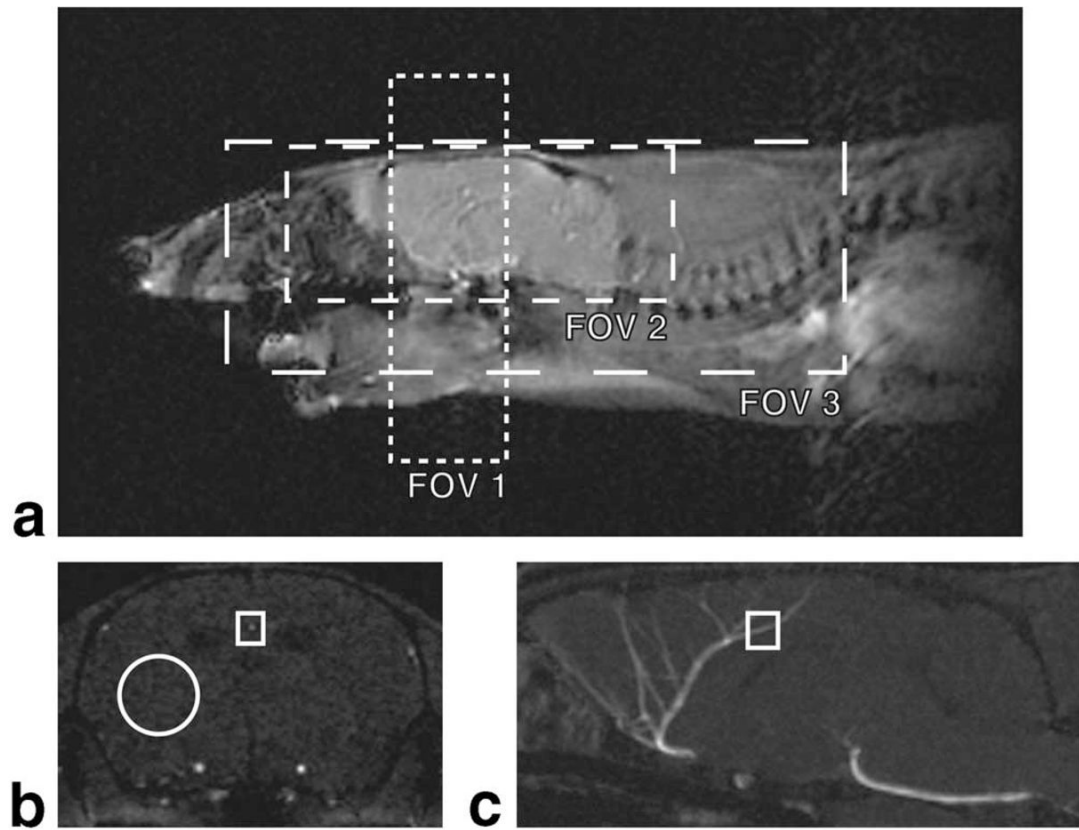
FIG. 1.
a: Localizer image showing the three FOV used. FOV 1 covered a thin 6-mm slab of the brain. FOV 2 covered the whole brain only. FOV 3 covered the entire neurovascular axis, including the aortic arch. **b,c:** An axial TOF-MRA slice and midsagittal MIP illustrating the ROIs used for the image analysis. Measurements were made on the axial images **(b)**. The vessel signal of the AzACA was the maximum intensity in the rectangular ROI. The tissue signal was the mean intensity in the round ROI. Measurements were made on all axial slices that intersected the 0.5-mm segment of AzACA marked in **(c)**.
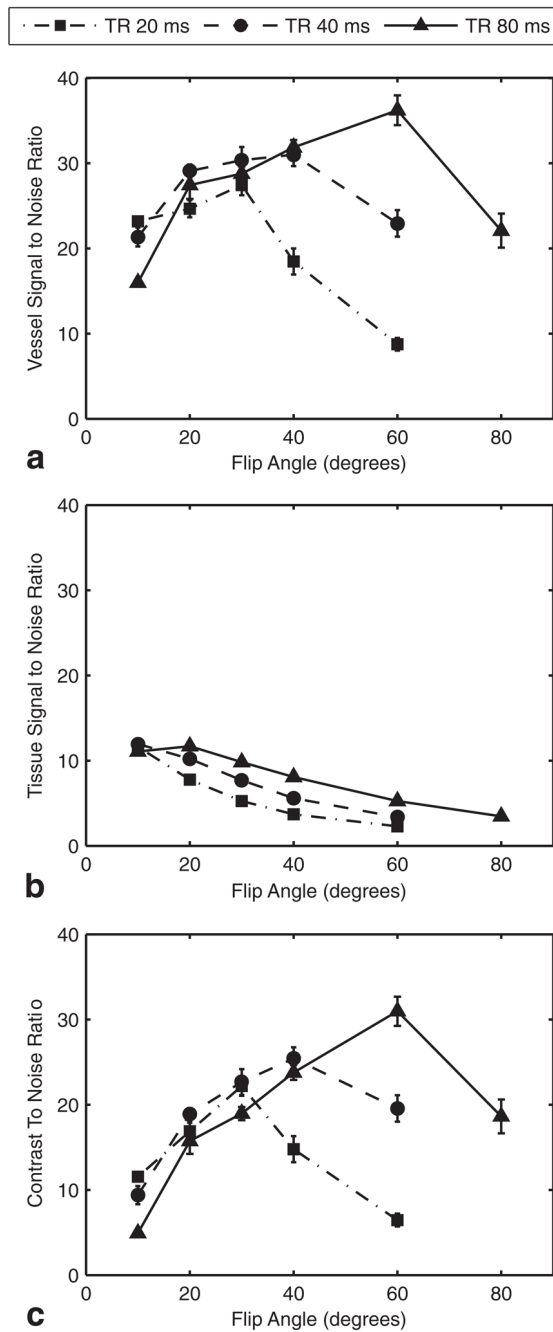
FIG. 2.
Optimization of TOF-MRA. **a:** The SNR in the 0.5-mm segment of the distal AzACA peaked at FA = 60° and TR = 80 ms. The long TR allowed the vessel to refill with unsaturated blood. **b:** The SNR of the background brain tissue decreased with increasing FA for all TRs. **c:** The CNR for the vessel was maximized, with FA = 60° and TR = 80 ms. The optimization was performed on three mice, with nearly identical results. For clarity, the plots are from a single specimen and show the mean ± standard error over the five slices through the 0.5-mm vessel segment. NEX were adjusted to equalize scan times.
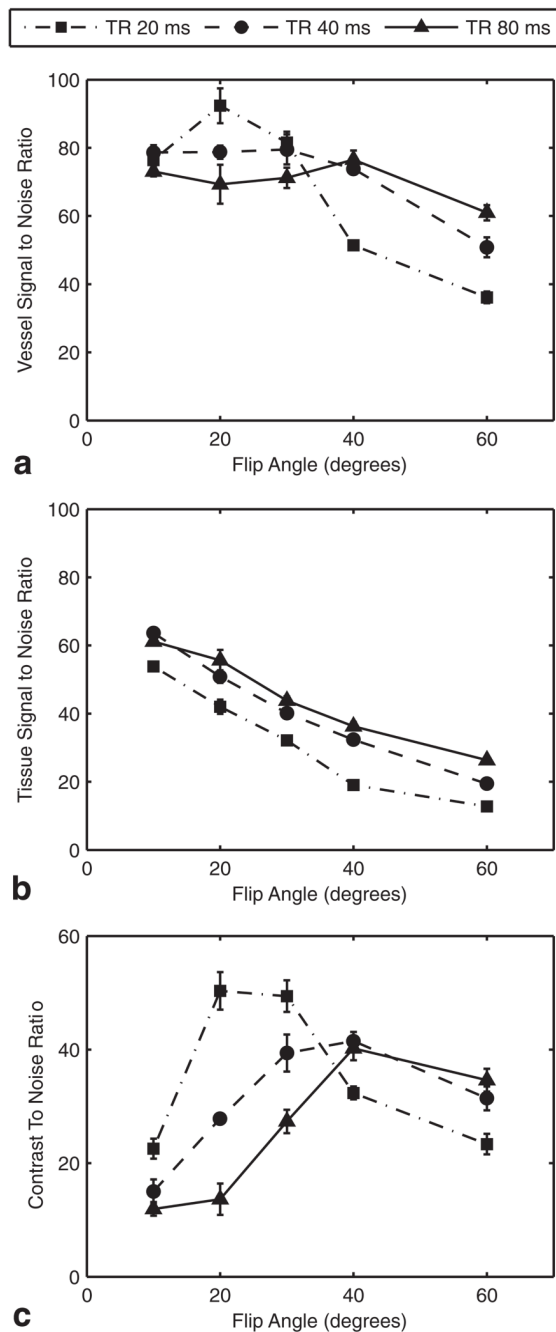
FIG. 3.
Optimization of CE-MRA with 0.08 mmol/kg SC-Gd liposomes. **a:** The SNR in the 0.5-mm segment of the distal AzACA peaked at FA = 20° and TR = 20 ms. **b:** The SNR of the background brain tissue decreased with increasing FA for all TRs. **c:** The CNR for the vessel was maximized, with FA = 20–30° and TR = 20 ms. The optimization was performed on three mice, with nearly identical results. For clarity, the plots are from a single specimen and show the mean ± standard error over the six slices through the 0.5-mm vessel segment. NEX were adjusted to equalize scan times.
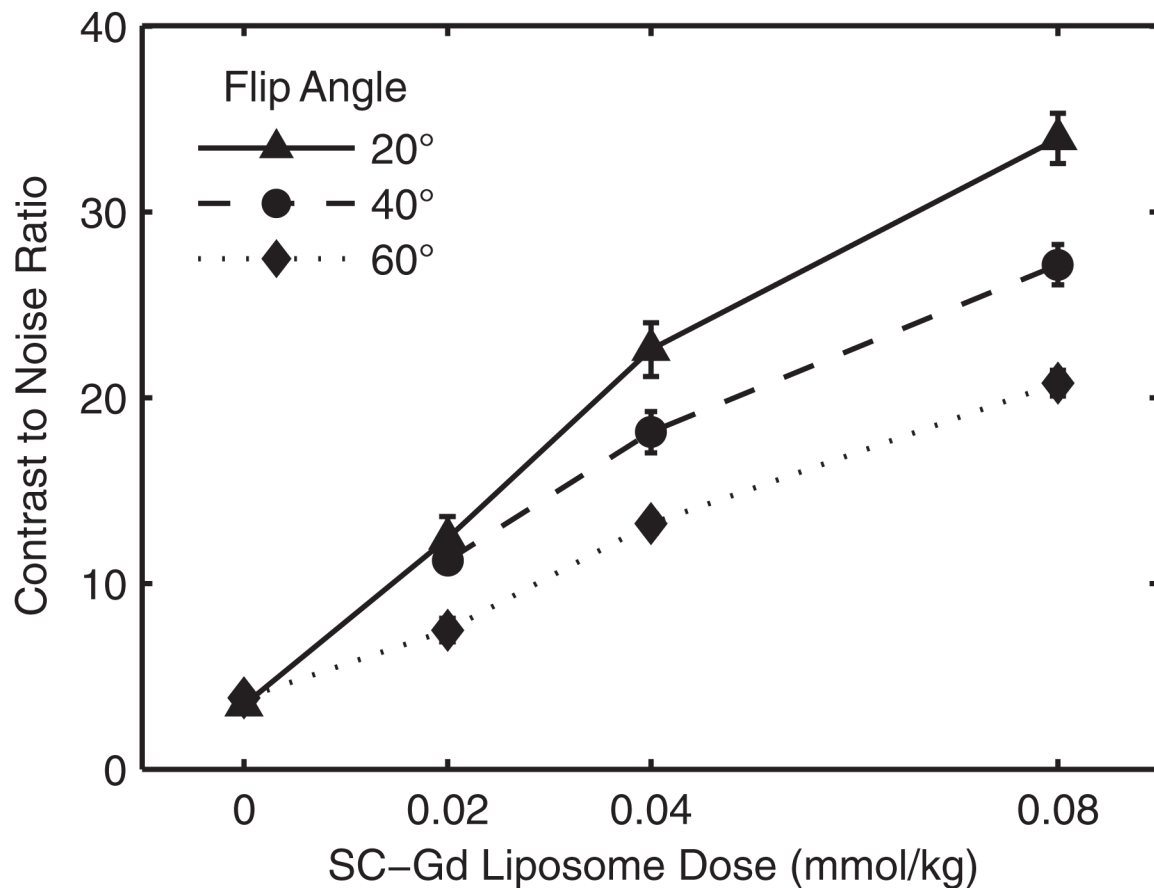
FIG. 4.
The effect of SC-Gd liposome dose on vessel CNR as measured in the superior sagittal sinus (vein). CNR increases dramatically as the SC-Gd liposome dose increases from 0 to 0.08 mmol Gd/kg bodyweight. However, the gain in CNR is steepest from 0 to 0.04 mmol/kg. The optimum TR of 20 ms was used over a range of FA. The plots show the CNR mean ± standard error over the five slices through the 0.5-mm vessel segment.
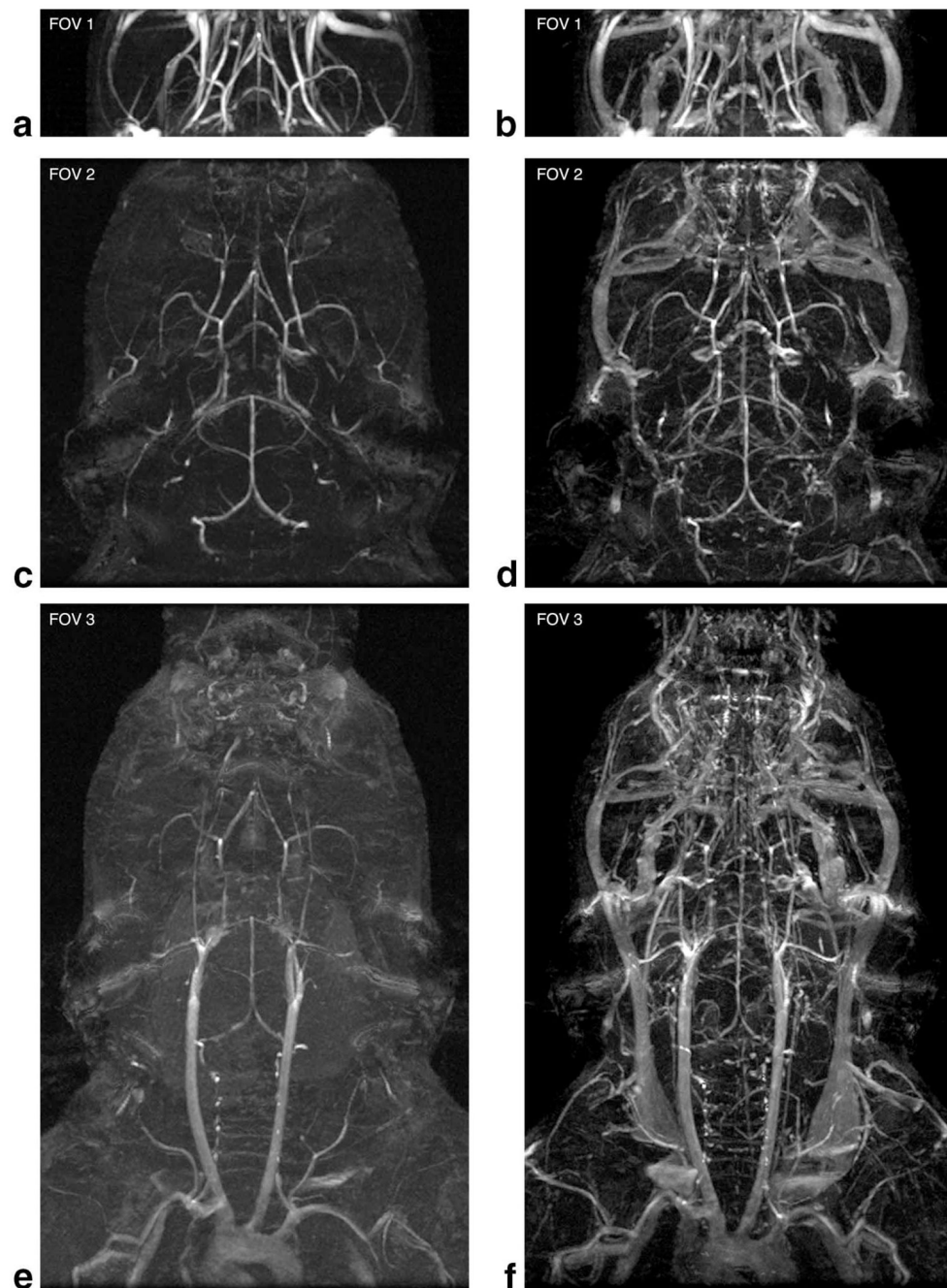
FIG. 5.
The effect of increasing FOV on vessel conspicuity for TOF-MRA **(a,c,e)** and CE-MRA with 0.08 mmol/kg SC-Gd liposomes **(b,d,f)**. At the very limited FOV 1, TOF-MRA has better small-vessel CNR than CE-MRA. However, as the FOV increases to include the whole brain (FOV 2) or the whole neurovascular axis (FOV 3), small-vessel CNR degrades dramatically in the TOF-MRA. All images shown are from a single specimen. The resolution was approximately $100 \times 100 \times 100 \ \mu m^3$ for all datasets. FOV and parameters are shown in Fig. 1 and Table 1.
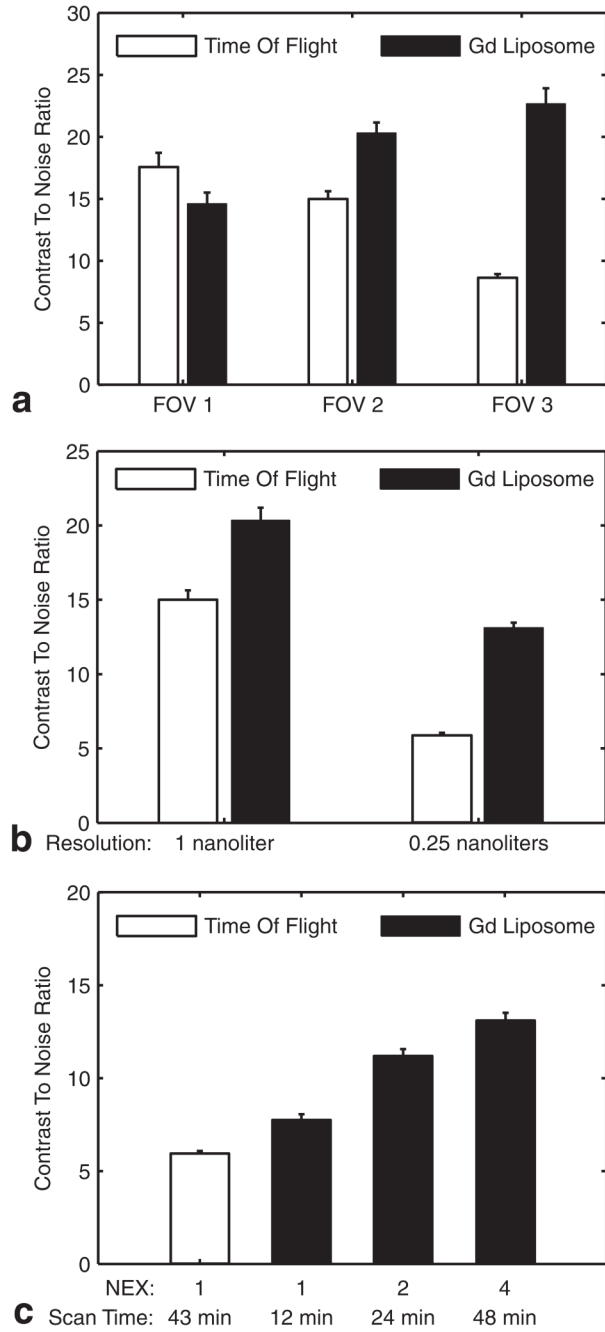
FIG. 6.
a: The effect of FOV (see Fig. 1) on the CNR of a distal segment of the AzACA. At FOV 1, the difference between TOF and SC-Gd liposomes is not significant ($P > 0.05$). As the FOV increases, the CNR of TOF-MRA decreases (despite increasing scan time), while the CE-MRA with 0.08 mmol/kg SC-Gd liposomes shows an increase in CNR. At FOVs 2 and 3, the SC-Gd liposomes give a significant ($P < 0.001$) increase in CNR. At each FOV, data were acquired with optimized parameters (Table 1) from a single specimen with NEX adjusted to equalize scan times. **b:** The effect of spatial resolution on the CNR of a distal segment of the AzACA indicates that SC-Gd liposomes have greater utility at higher spatial resolution. At 1-nL resolution, SC-Gd liposomes ($n = 1$) provide a 36% benefit ($P < 0.001$) in CNR over TOF (n

= 1). However, as the resolution increases 4-fold to 0.27 nL, the SC-Gd ($n = 5$) advantage ($P < 0.001$) increases to 123% over TOF ($n = 9$). At each resolution, data were acquired with optimized parameters from FOV 2, with NEX adjusted to equalize scan times. **c:** The effect of reduced NEX (scan time) on the CNR of the distal AzACA. The optimum TR for TOF-MRA was 80 ms, but for CE-MRA it was 20 ms. Thus, for a given resolution, CE-MRA scan time could be reduced by using fewer NEX. Compared to TOF-MRA ($n = 9$), CE-MRA ($n = 1$) has 32% higher CNR ($P < 0.001$), even with scan time reduced by 75% to 12 min. Data were acquired with optimized parameters from FOV 2 at a resolution of 0.27 nL. All figures: plots show CNR mean ± standard error of the mean over the axial slices from the 0.5-mm segment of the AzACA.
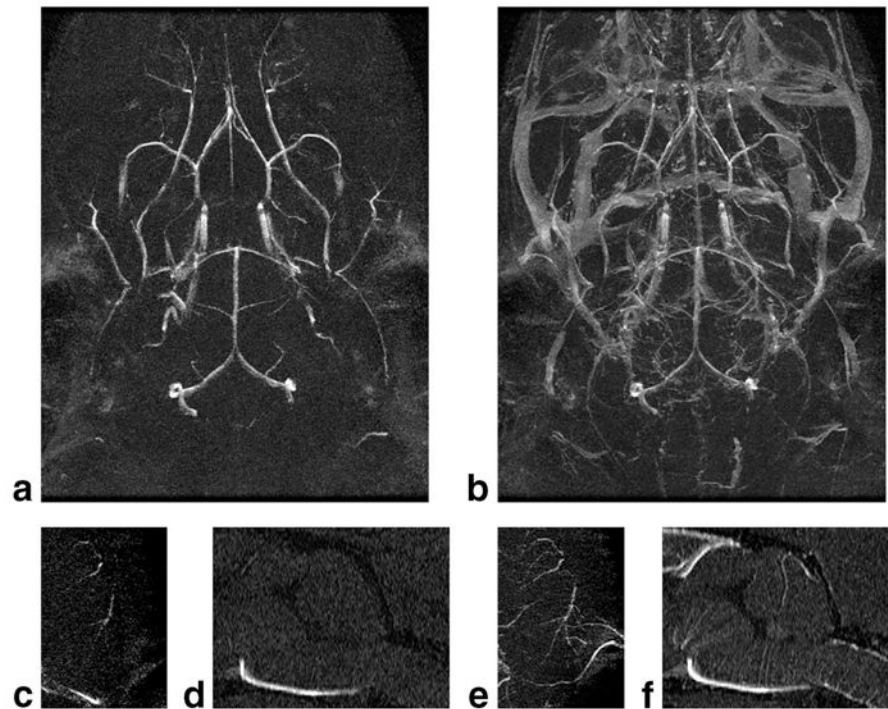
FIG. 7.
High-resolution MRA of the mouse brain acquired with TOF or SC-Gd liposome contrast. Spatial resolution is $52 \times 52 \times 100\ \mu m^3$ (0.27 nL). **a,b:** MIPs of the whole brain. Note that CE-MRA shows the venous structures as well. **c,e:** MIPs of 1-mm dorsalmost slab of the brain reveal the distal branches of the middle cerebral artery. SC-Gd demonstrates a greater extent of the vessel. **d,f:** MIPs of the 0.3-mm mid-sagittal slab of the rostral brain reveal the very fine perforating branches of the anterior spinal artery and basilar artery. Again, SC-Gd more clearly demonstrates the finest vessels.

Table 1

SPGR Scan Parameters Used to Evaluate the Effect of FOV on TOF and CE-MRA

Anatomy	FOV (mm^3)	Matrix	TOF parameters				SC-Gd parameters			
			TE (ms)	TR (ms)	FA (°)	NEX	TE (ms)	TR (ms)	FA (°)	NEX
FOV 1	Slab of brain and neck	20 × 20 × 6	192 × 192 × 603	80	60	1	3	20	20	4
FOV 2	Whole brain	20 × 20 × 8	192 × 192 × 803	80	60	1	3	20	20	4
FOV 3	Neurovascular axis	32 × 32 × 12	320 × 320 × 120	3	80	60	1	3	20	20	4